Advances in Applied Mathematics and Mechanics
Adv. Appl. Math. Mech., Vol. **4**, No. 3, pp. 340-353

DOI: 10.4208/aamm.10-m11142
June 2012

Modifying and Reducing Numerical Dissipation in A Two-Dimensional Central-Upwind Scheme

Chi-Jer Yu[1,*] and Chii-Tung Liu[2]

[1] *Department of Applied Mathematics, National Chiao Tung University, 1001 University Road, Hsinchu 300, Taiwan*
[2] *Department of Computer Science and Information Engineering, Chaoyang University of Technology, 168 Jifong E. Rd., Wufong Township Taichung County 41349, Taiwan*

Received 11 September; Accepted (in revised version) 10 October 2011

Available online 30 April 2012

Abstract. This study presents a modification of the central-upwind Kurganov scheme for approximating the solution of the 2D Euler equation. The prototype, extended from a 1D model, reduces substantially less dissipation than expected. The problem arises from over-restriction of some slope limiters, which keep slopes between interfaces of cells to be Total-Variation-Diminishing. This study reports the defect and presents a re-derived optimal formula. Numerical experiments highlight the significance of this formula, especially in long-time, large-scale simulations.

AMS subject classifications: 76T05,65M05

Key words: Hyperbolic systems of conservation laws, Godunov-type finite-volume methods, central-upwind scheme, Kurganov, numerical dissipation, anti-diffusion.

1 Introduction

This study simulates the dynamics of ideal gas based on conservation laws for mass, momentum and energy, which are described by the hyperbolic system of Euler equations. Over the last three to four decades, researchers have presented many schemes and improved greatly in this field [9]. The central-upwind (Riemann-problem-solver-free and central Godunov-type projection-evolution) methods [2–8, 11–13] offer impressive advances with key features that bypass solving of the Riemann problem and therefore simplify complex and heavy computations. The central-upwind framework also significantly decreases the numerical dissipation present in the staggered central schemes. They were improved progressively by more precise estimates of the width

*Corresponding author.
URL: http://www.math.nctu.edu.tw/faculty/e_faculty_content.php?S_ID=31&SC_ID=1
Email: ycj@math.nctu.edu.tw (C. J. Yu)

of Riemann fans[†] and a higher order of interpolation with sharper slopes to reconstruct cell distributions. Finally, semi-discrete configurations facilitate multidimensional extensions substantially. As described in [2], this series of algorithms enjoys the advantages of high resolution, simplicity, universality and robustness.

Despite lighter loading, it took at least 320 CPU hours to complete one round of computation for the 2D Rayleigh-Taylor instability problem with 1728×6912 grids. Such time-consuming experiments motivate the use of newest massively parallel computing technique, GPGPU (General purpose computing with graphics processor units). The most valuable feature of a GPU is its large number of scalar processors (SPs) which offer much better computing performance than a CPU (GPU $\approx$ 1000GFLOPS vs. CPU $<$ 10GFLOPS). Here GFLOPS means Giga (one billion) Floating point Operations Per Second. However, the cost is a whole new programming strategy under special structures [15, 16, 19–22].

In this application, we tried several revised configurations and found that the anti-diffusion term (2.5) is the key to improving computing accuracy near discontinuities. Whereas the dissipation reducing is not easily observed over a short period or at a low resolution, the powerful GPU can perform one round of simulation within 13.5 hours. This makes it possible to investigate the ultimate effects of the anti-diffusion mechanism.

In solving 1D Euler equations, the prototype [2] keeps discontinuities as narrow as possible. However, it shows signs of weakness when simulating 2D Euler equations. This is caused by over-operation of some slope limiters in formula (2.3a), whose original purpose is to restrict, under Total-Variation-Diminishing (TVD) conditions, the slopes between interfaces of cells to avoid oscillations. This study analyzes what happens, re-derives a modified formula in Section 3 and finally demonstrates its significance with a series of large-scale numerical simulations in Section 4.

2 Numerical algorithm

The 2D Euler equations can be written as

$$\mathbf{U}_t + f(\mathbf{U})_x + g(\mathbf{U})_y = s(\mathbf{U}), \tag{2.1}$$

where

$$\begin{aligned}
&\mathbf{U}(x,y,t) = (\rho, \rho u, \rho v, E),\\
&f(\mathbf{U}) = f(\rho, \rho u, \rho v, E) = (\rho u, \rho u^2 + P, \rho uv, u(E+P)),\\
&g(\mathbf{U}) = (\rho v, \rho uv, \rho v^2 + P, v(E+P)).
\end{aligned}$$

Here $\rho(x,y,t)$ is the density, $(u(x,y,t), v(x,y,t))$ is the velocity, $E(x,y,t)$ is the total energy and $P(x,y,t)$ is the pressure. The relationship between is

$$E = \frac{P}{\gamma - 1} + \frac{1}{2}P(u^2 + v^2);$$

[†]The fan area is caused by the propagation of discontinuity from the initial state.

where γ is a constant depending on the species of the gas and $s(\mathbf{U})$ is the source term.

2.1 Prototype

The semi-discrete type of Kurganov scheme [2] is to integrate the following O.D.E. system:

$$\frac{d}{dt}\mathbf{U}_{ij}(t) = -\frac{\mathbf{F}_{i,j+\frac{1}{2}}(t) - \mathbf{F}_{i,j-\frac{1}{2}}(t)}{\Delta x} - \frac{\mathbf{G}_{i+\frac{1}{2},j}(t) - \mathbf{G}_{i-\frac{1}{2},j}(t)}{\Delta y} + s(\mathbf{U}_{ij}(t)), \tag{2.2a}$$

$$\mathbf{F}_{i,j+\frac{1}{2}}(t) = \frac{a^+_{i,j+\frac{1}{2}} f(\mathbf{U}^{\mathrm{E}}_{i,j}) - a^-_{i,j+\frac{1}{2}} f(\mathbf{U}^{\mathrm{W}}_{i,j+1})}{a^+_{i,j+\frac{1}{2}} - a^-_{i,j+\frac{1}{2}}} + a^+_{i,j+\frac{1}{2}} \cdot a^-_{i,j+\frac{1}{2}} \Big[\frac{\mathbf{U}^{\mathrm{W}}_{i,j+1} - \mathbf{U}^{\mathrm{E}}_{i,j}}{a^+_{i,j+\frac{1}{2}} - a^-_{i,j+\frac{1}{2}}} - \mathbf{Q}^x_{i,j+\frac{1}{2}}\Big], \tag{2.2b}$$

$$\mathbf{G}_{i+\frac{1}{2},j}(t) = \frac{b^+_{i+\frac{1}{2},j} g(\mathbf{U}^{\mathrm{N}}_{i,j}) - b^-_{i+\frac{1}{2},j} g(\mathbf{U}^{\mathrm{S}}_{i+1,j})}{b^+_{i+\frac{1}{2},j} - b^-_{i+\frac{1}{2},j}} + b^+_{i+\frac{1}{2},j} \cdot b^-_{i+\frac{1}{2},j} \Big[\frac{\mathbf{U}^{\mathrm{S}}_{i+1,j} - \mathbf{U}^{\mathrm{N}}_{i,j}}{b^+_{i+\frac{1}{2},j} - b^-_{i+\frac{1}{2},j}} - \mathbf{Q}^y_{i+\frac{1}{2},j}\Big], \tag{2.2c}$$

$$a^+_{i,j+\frac{1}{2}} = \max(0, \lambda^+_x(\mathbf{U}^{\mathrm{W}}_{i,j+1}), \lambda^+_x(\mathbf{U}^{\mathrm{E}}_{i,j})), \qquad a^-_{i,j+\frac{1}{2}} = \min(0, \lambda^-_x(\mathbf{U}^{\mathrm{W}}_{i,j+1}), \lambda^-_x(\mathbf{U}^{\mathrm{E}}_{i,j})), \tag{2.2d}$$

$$b^+_{i+\frac{1}{2},j} = \max(0, \lambda^+_y(\mathbf{U}^{\mathrm{S}}_{i+1,j}), \lambda^+_y(\mathbf{U}^{\mathrm{N}}_{i,j})), \qquad b^-_{i+\frac{1}{2},j} = \min(0, \lambda^-_y(\mathbf{U}^{\mathrm{S}}_{i+1,j}), \lambda^-_y(\mathbf{U}^{\mathrm{N}}_{i,j})), \tag{2.2e}$$

$$\lambda^\pm_x(\mathbf{U}) = u \pm \sqrt{\gamma P/\rho} \text{ are the slowest and fastest eigenvalues of } \frac{\partial f}{\partial \mathbf{U}}, \tag{2.2f}$$

$$\lambda^\pm_y(\mathbf{U}) = v \pm \sqrt{\gamma P/\rho} \text{ are the slowest and fastest eigenvalues of } \frac{\partial g}{\partial \mathbf{U}}, \tag{2.2g}$$

$$\mathbf{U}^{\mathrm{E(W)}}_{i,j} = p_{i,j}\Big(x_j \pm \frac{\Delta x}{2}, y_i\Big), \qquad \mathbf{U}^{\mathrm{N(S)}}_{i,j} = p_{i,j}\Big(x_j, y_i \pm \frac{\Delta y}{2}\Big), \tag{2.2h}$$

where $p_{i,j}(x,y)$ is a linear interpolant defined in the interval $[x_j - \Delta x/2, x_j + \Delta x/2] \times [y_i - \Delta y/2, y_i + \Delta y/2]$ which can be used to reconstruct $\mathbf{U}(x,y,t_n)$ in a neighborhood of (x_j, y_i) at time t_n

$$\mathbf{Q}^x_{i,j+\frac{1}{2}} = \frac{\mathrm{minmod}\big(\mathbf{U}^{\mathrm{NW}}_{i,j+1} - w^{\mathrm{int}}_{i,j+\frac{1}{2}}, \mathbf{U}^{\mathrm{SW}}_{i,j+1} - w^{\mathrm{int}}_{i,j+\frac{1}{2}}, w^{\mathrm{int}}_{i,j+\frac{1}{2}} - \mathbf{U}^{\mathrm{NE}}_{i,j}, w^{\mathrm{int}}_{i,j+\frac{1}{2}} - \mathbf{U}^{\mathrm{SE}}_{i,j}\big)}{a^+_{i,j+\frac{1}{2}} - a^-_{i,j+\frac{1}{2}}}, \tag{2.3a}$$

$$\mathbf{Q}^y_{i+\frac{1}{2},j} = \frac{\mathrm{minmod}\big(\mathbf{U}^{\mathrm{SW}}_{i+1,j} - w^{\mathrm{int}}_{i+\frac{1}{2},j}, \mathbf{U}^{\mathrm{SE}}_{i+1,j} - w^{\mathrm{int}}_{i+\frac{1}{2},j}, w^{\mathrm{int}}_{i+\frac{1}{2},j} - \mathbf{U}^{\mathrm{NW}}_{i,j}, w^{\mathrm{int}}_{i+\frac{1}{2},j} - \mathbf{U}^{\mathrm{NE}}_{i,j}\big)}{b^+_{i+\frac{1}{2},j} - b^-_{i+\frac{1}{2},j}}, \tag{2.3b}$$

$$\mathrm{minmod}(c_1, \cdots, c_m) = \begin{cases} \min(c_1, \cdots, c_m), & \text{if } c_i > 0 \ \forall i = 1, \cdots, m, \\ \max(c_1, \cdots, c_m), & \text{if } c_i < 0 \ \forall i = 1, \cdots, m, \\ 0, & \text{otherwise.} \end{cases} \tag{2.3c}$$

$\mathbf{Q}^x_{i,j+1/2}$ and $\mathbf{Q}^y_{i+1/2,j}$ are the anti-diffusion terms which contribute to reduce numerical

dissipation.

$$\mathbf{U}_{i,j}^{\mathrm{NE(NW)}} = p_{i,j}\Big(x_j \pm \frac{\Delta x}{2}, y_i + \frac{\Delta y}{2}\Big), \qquad \mathbf{U}_{i,j}^{\mathrm{SE(SW)}} = p_{i,j}\Big(x_j \pm \frac{\Delta x}{2}, y_i - \frac{\Delta y}{2}\Big),$$

$$w_{i,j+\frac{1}{2}}^{\mathrm{int}} = \frac{a_{i,j+\frac{1}{2}}^{+}\mathbf{U}_{i,j+1}^{\mathrm{W}} - a_{i,j+\frac{1}{2}}^{-}\mathbf{U}_{i,j}^{\mathrm{E}} + f(\mathbf{U}_{i,j+1}^{\mathrm{W}}) - f(\mathbf{U}_{i,j}^{\mathrm{E}})}{a_{i,j+\frac{1}{2}}^{+} - a_{i,j+\frac{1}{2}}^{-}},$$

$$w_{i+\frac{1}{2},j}^{\mathrm{int}} = \frac{b_{i+\frac{1}{2},j}^{+}\mathbf{U}_{i+1,j}^{\mathrm{S}} - b_{i+\frac{1}{2},j}^{-}\mathbf{U}_{i,j}^{\mathrm{N}} + g(\mathbf{U}_{i+1,j}^{\mathrm{S}}) - g(\mathbf{U}_{i,j}^{\mathrm{N}})}{b_{i+\frac{1}{2},j}^{+} - b_{i+\frac{1}{2},j}^{-}}.$$

To integrate the ODE (2.2a), each time step is restricted by the CFL-condition, i.e.,

$$t_{n+1} - t_n = \Delta t \le CFL \cdot \min_{i,j}\left(\frac{\Delta x}{\max\left(a_{j+\frac{1}{2}}^{+}, -a_{j+\frac{1}{2}}^{-}\right)}, \frac{\Delta y}{\max\left(b_{i+\frac{1}{2}}^{+}, -b_{i+\frac{1}{2}}^{-}\right)}\right).$$

The key difference between this algorithm (2.2c) and others [3,4,7,8] is the presence of additional anti-diffusion terms (2.3a). These terms can improve computing accuracy near discontinuities, as illustrated by the figures in Section 4.

2.2 Simplified form

As mentioned by Remark 4.1 in [2], formula (2.2a) is "almost" dimension-separable; the directional flux $(F_{i,j+1/2}(t) - F_{i,j-1/2}(t))/\Delta x$ and $(\mathbf{G}_{i+1/2,j}(t) - \mathbf{G}_{i-1/2,j}(t))/\Delta y$ seem to depend only on $f(\mathbf{U})$ and $g(\mathbf{U})$ individually without interaction. However, the anti-diffusion terms (2.3a) $\mathbf{Q}_{i,j+1/2}^{x}$ and $\mathbf{Q}_{i+1/2,j}^{y}$ contain $\mathbf{U}_{i,j}^{\mathrm{NE(NW)}}$ and $\mathbf{U}_{i,j}^{\mathrm{SE(SW)}}$, which must refer to both $f(\mathbf{U})$ and $g(\mathbf{U})$. It is not possible to evaluate independently the directional flux (with respect to the partial derivative) within each dimension. To some degree, this prevents parallel computing.

Consider departing the 2D model (2.1) in dimension-separated sense, that is, attempt to evaluate $\mathbf{Q}_{i,j+1/2}^{x}$ and $\mathbf{Q}_{i+1/2,j}^{y}$ in only one-dimensional form

$$\mathbf{Q}_{i,j+\frac{1}{2}}^{x} = \frac{\mathrm{minmod}\big(\mathbf{U}_{i,j+1}^{\mathrm{W}} - w_{i,j+\frac{1}{2}}^{\mathrm{int}}, w_{i,j+\frac{1}{2}}^{\mathrm{int}} - \mathbf{U}_{i,j}^{\mathrm{E}}\big)}{a_{i,j+\frac{1}{2}}^{+} - a_{i,j+\frac{1}{2}}^{-}}, \tag{2.4a}$$

$$\mathbf{Q}_{i+\frac{1}{2},j}^{y} = \frac{\mathrm{minmod}\big(\mathbf{U}_{i+1,j}^{\mathrm{S}} - w_{i+\frac{1}{2},j}^{\mathrm{int}}, w_{i+\frac{1}{2},j}^{\mathrm{int}} - \mathbf{U}_{i,j}^{\mathrm{N}}\big)}{b_{i+\frac{1}{2},j}^{+} - b_{i+\frac{1}{2},j}^{-}}. \tag{2.4b}$$

This approach is just like using the 1D algorithm in [2, 6] to solve for the flux $\mathbf{F}$ and $\mathbf{G}$ in two dimensions individually and then combining their outcomes. This approach works in parallel and is much easier. However, such a simplified limitation of slope may violate the premier TVD objective and result in extraneous oscillations.

As mentioned in Section 1, $\mathbf{Q}_{i,j+1/2}^{x}$ and $\mathbf{Q}_{i+1/2,j}^{y}$ are the major keys in the Kurganov scheme. A little variation will subvert thoroughly its accuracy. Section 4 demonstrates different figures w.r.t. the utilization of different anti-diffusion terms.

2.3 Modified form

The original anti-diffusion terms (2.3a) have little effect on practical 2D simulations. Instead, it is formula (2.4) that makes a great difference. The problem arises from some over limitation of slopes. Below is an alternative of anti-diffusion terms which we will demonstrate as a moderate modification for those of (2.3a) or (2.4). Section 3 analyzes these three formulas

$$\mathbf{Q}^x_{i,j+\frac{1}{2}} = \frac{\text{minmod}\Big(\mathbf{U}^{\text{W}}_{i,j+1} - w^{\text{int}}_{i,j+\frac{1}{2}}, w^{\text{int}}_{i,j+\frac{1}{2}} - \mathbf{U}^{\text{E}}_{i,j}, \frac{\mathbf{U}^{\text{NW}}_{i,j+1}-\mathbf{U}^{\text{NE}}_{i,j}}{2}, \frac{\mathbf{U}^{\text{SW}}_{i,j+1}-\mathbf{U}^{\text{SE}}_{i,j}}{2}\Big)}{a^+_{i,j+\frac{1}{2}} - a^-_{i,j+\frac{1}{2}}}, \tag{2.5a}$$

$$\mathbf{Q}^y_{i+\frac{1}{2},j} = \frac{\text{minmod}\Big(\mathbf{U}^{\text{S}}_{i+1,j} - w^{\text{int}}_{i+\frac{1}{2},j}, w^{\text{int}}_{i+\frac{1}{2},j} - \mathbf{U}^{\text{N}}_{i,j}, \frac{\mathbf{U}^{\text{SW}}_{i+1,j}-\mathbf{U}^{\text{NW}}_{i,j}}{2}, \frac{\mathbf{U}^{\text{SE}}_{i+1,j}-\mathbf{U}^{\text{NE}}_{i,j}}{2}\Big)}{b^+_{i+\frac{1}{2},j} - b^-_{i+\frac{1}{2},j}}. \tag{2.5b}$$

3 Derivation of modification

To demonstrate the proposed modification, this section first briefly explains the intension of formula (2.3a) and then provides a detailed revaluation using Figs. 1 and 2. Finally, this section compares formulas (2.3a), (2.4) and (2.5).

Reconstructing $\mathbf{U}(x, y, t_n)$ with as steep as possible linear planes on $D_{i,j+1/2}$ and $D_{i+1/2,j}$ reduces the numerical dissipations between cell interfaces. For $D_{i,j+1/2}$, for example, the four values $\mathbf{U}^{\text{SW(NW)}}_{i,j+1}$, $\mathbf{U}^{\text{SE(NE)}}_{i,j}$ at corners $P_1, \cdots, P_4$ and the average $w^{\text{int}}_{i,j+1/2}$ are involved in the interpolation to determine $(\mathbf{U}_x)^{n+1}_{i,j+1/2}$ and $(\mathbf{U}_y)^{n+1}_{i,j+1/2}$, the plane's x-slope and y-slope. As mentioned in [2,8], the x-slope is a real anti-diffusion key. In contrast, the y-slope has no effect by the subsequent projection average. However, the latter interferes with the availability of the former and causes either in formula (2.3a) to over-exclude some feasible solutions or in formula (2.4) to connive the controversial solutions.

For brevity, the following discussion omits the subscript if there is no confusion. We now show how to determine the optimal $\mathbf{U}_x$, i.e., $(\mathbf{U}_x)^{n+1}_{i,j+1/2}$, with computed U^{E}, U^{W}, U^{SE}, U^{SW}, U^{NE}, U^{NW} and w^{int} under TVD constraint.

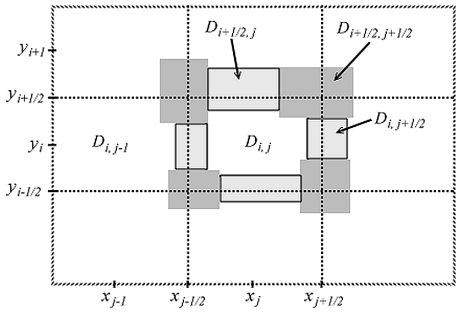

Figure 1: Non-uniform location of control volumes in 2D model, as Fig. 3 in [2].

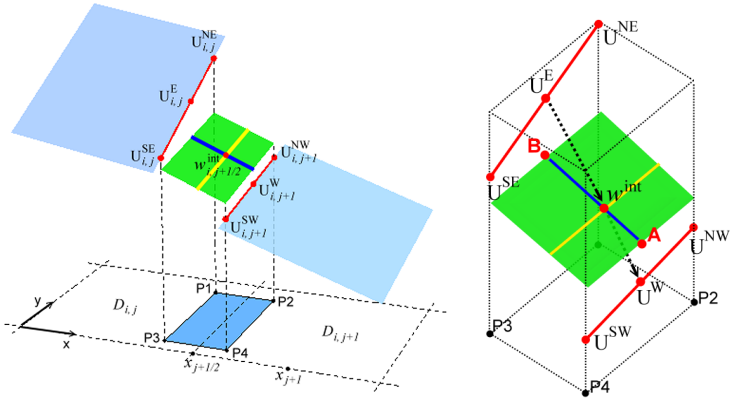

Figure 2: 3D view of control volumes with interpolation planes on the interfaces of cells.

Without loss of generality, assume that $\mathrm{U}^{\mathrm{E}} \geq w^{\mathrm{int}} \geq \mathrm{U}^{\mathrm{W}}$. Let

$$\delta x = \frac{1}{2}\overline{\mathrm{P_3P_4}} = \frac{1}{2}\left(a^{+}_{i,j+\frac{1}{2}} - a^{-}_{i,j+\frac{1}{2}}\right)\cdot \Delta t, \qquad \delta y = \frac{1}{2}\overline{\mathrm{P_2P_4}}.$$

$\mathbf{U}_x$ is the slope of the blue line on the green plane, which must be TVD restrained in the x-direction,

$$\mathbf{U}_x = \min \mathrm{mod}\left(\frac{\mathrm{U}^{\mathrm{W}} - w^{\mathrm{int}}}{\delta x}, \frac{w^{\mathrm{int}} - \mathrm{U}^{\mathrm{E}}}{\delta x}\right),$$

i.e.,

$$\frac{\mathrm{U}^{\mathrm{W}} - w^{\mathrm{int}}}{\delta x} \leq \mathbf{U}_x \leq 0, \qquad \frac{w^{\mathrm{int}} - \mathrm{U}^{\mathrm{E}}}{\delta x} \leq \mathbf{U}_x \leq 0. \tag{3.1}$$

$\mathbf{U}_y$ is the slope of the yellow line on the green plane, which must be TVD restrained in the y-direction. Therefore, on the vertical plane P2-P4,

$$\mathbf{U}_y \in \left[\frac{\mathrm{U}^{\mathrm{NW}} - \mathrm{A}}{\delta y}, \frac{\mathrm{A} - \mathrm{U}^{\mathrm{SW}}}{\delta y}\right]. \tag{3.2}$$

Remark 3.1. On the intersection of the green plane and plane P2-P4,

$$\mathrm{A} = w^{\mathrm{int}} + \delta x \cdot \mathbf{U}_x + 0 \cdot \mathbf{U}_y \geq \mathrm{U}^{\mathrm{W}} = \frac{\mathrm{U}^{\mathrm{NW}} + \mathrm{U}^{\mathrm{SW}}}{2},$$

by (3.1). Therefore

$$\mathrm{U}^{\mathrm{NW}} - \mathrm{A} \leq \mathrm{A} - \mathrm{U}^{\mathrm{SW}},$$

and then,

$$\frac{\mathrm{U}^{\mathrm{NW}} - \mathrm{A}}{\delta y} \leq \frac{\mathrm{A} - \mathrm{U}^{\mathrm{SW}}}{\delta y}.$$

Similarly, on the vertical plane P1-P3,

$$\mathbf{U}_y \in \Big[\frac{\mathrm{B}-\mathrm{U}^{\mathrm{SE}}}{\delta y}, \frac{\mathrm{U}^{\mathrm{NE}}-\mathrm{B}}{\delta y}\Big]. \tag{3.3}$$

The conditions (3.1), (3.2) and (3.3) must be fully satisfied to guarantee the TVD property in both the x-direction and y-direction. Intervals in (3.2) and (3.3) both depend on the value of $\mathbf{U}_x$. If there is no intersection between these two intervals, a moderate $\mathbf{U}_y$ is not possible. In other words, extreme values of feasible $\mathbf{U}_x$ will occur when the two intervals intersect at only one point.

That is, either

$$\frac{\mathrm{A}-\mathrm{U}^{\mathrm{SW}}}{\delta y} = \frac{\mathrm{B}-\mathrm{U}^{\mathrm{SE}}}{\delta y} \quad \text{or} \quad \frac{\mathrm{U}^{\mathrm{NW}}-\mathrm{A}}{\delta y} = \frac{\mathrm{U}^{\mathrm{NE}}-\mathrm{B}}{\delta y},$$
$$w^{\mathrm{int}} + \delta x\cdot\mathbf{U}_x - \mathrm{U}^{\mathrm{SW}} = w^{\mathrm{int}} - \delta x\cdot\mathbf{U}_x - \mathrm{U}^{\mathrm{SE}} \Rightarrow \mathbf{U}_x = \frac{\mathrm{U}^{\mathrm{SW}}-\mathrm{U}^{\mathrm{SE}}}{2\delta x},$$
$$\mathrm{U}^{\mathrm{NW}} - (w^{\mathrm{int}} + \delta x\cdot\mathbf{U}_x) = \mathrm{U}^{\mathrm{NE}} - (w^{\mathrm{int}} - \delta x\cdot\mathbf{U}_x) \Rightarrow \mathbf{U}_x = \frac{\mathrm{U}^{\mathrm{NW}}-\mathrm{U}^{\mathrm{NE}}}{2\delta x}.$$

Therefore

$$\mathbf{U}_x = \min\,\mathrm{mod}\Big(\frac{\mathrm{U}^{\mathrm{SW}}-\mathrm{U}^{\mathrm{SE}}}{2\delta x}, \frac{\mathrm{U}^{\mathrm{NW}}-\mathrm{U}^{\mathrm{NE}}}{2\delta x}\Big). \tag{3.4}$$

Ignoring the feasibility of $\mathbf{U}_y$ by considering only (3.1) leads to formula (2.4) after passing to the semi-discrete limit. In contrast, synthesizing (3.1) and (3.4) generates formula (2.5). If $\mathbf{U}_y$ is set to zero, then (3.2) and (3.3) show that

$$\frac{\mathrm{U}^{\mathrm{NW}}-\mathrm{A}}{\delta y} \le 0 \le \frac{\mathrm{A}-\mathrm{U}^{\mathrm{SW}}}{\delta y} \Rightarrow \mathbf{U}_x \ge \frac{\mathrm{U}^{\mathrm{NW}}-w^{\mathrm{int}}}{\delta x} \text{ and } \mathbf{U}_x \ge \frac{\mathrm{U}^{\mathrm{SW}}-w^{\mathrm{int}}}{\delta x},$$
$$\frac{\mathrm{B}-\mathrm{U}^{\mathrm{SE}}}{\delta y} \le 0 \le \frac{\mathrm{U}^{\mathrm{NE}}-\mathrm{B}}{\delta y} \Rightarrow \mathbf{U}_x \ge \frac{w^{\mathrm{int}}-\mathrm{U}^{\mathrm{SE}}}{\delta x} \text{ and } \mathbf{U}_x \ge \frac{w^{\mathrm{int}}-\mathrm{U}^{\mathrm{NE}}}{\delta x}.$$

Therefore,

$$\mathbf{U}_x = \min\,\mathrm{mod}\Big(\frac{\mathrm{U}^{\mathrm{NW}}-w^{\mathrm{int}}}{\delta x}, \frac{\mathrm{U}^{\mathrm{SW}}-w^{\mathrm{int}}}{\delta x}, \frac{w^{\mathrm{int}}-\mathrm{U}^{\mathrm{SE}}}{\delta x}, \frac{w^{\mathrm{int}}-\mathrm{U}^{\mathrm{NE}}}{\delta x}\Big). \tag{3.5}$$

The outcome condition (3.5) leads to formula (2.3a).

Formula (2.4) may violate the TVD constraint. However, formula (2.5) is a restrained version of the former that considers 2 more quantities. In contrast, the implicit precondition $\mathbf{U}_y = 0$ makes (3.5) unduly prudent in determining a feasible nonzero $\mathbf{U}_x$. Consequently in (2.3a), $\mathbf{Q}^x_{i,j+1/2} = 0$ and (2.2c) degenerates back to scheme [3,4,7,8]. In conclusion, (2.5) is the optimal feasible choice of $\mathbf{U}_x$. Section 4 surveys the practical evidence for discrepancy and efficacy between those formulas by numerical simulations.

4 Numerical simulations

ODE (2.2a) should be better to integrate with a 3rd-order SSP/TVD ODE solver [17, 18], as suggested in [2]. Because the enhanced anti-diffusion terms only work near discontinuities, we simply test unsmooth problems to demonstrate the effects induced by different formulas (2.3a), (2.4) and (2.5). Tables 1 and 2 below specify the simulation environment and execution times.

Table 1: Specifications of the test platforms.

System Hardware			
PC	CPU	Intel Core 2 Duo E8500	3.16GHz, 6MB L2 Cache, FSB-1333 MHz
	Host RAM		4×2048 MB DDR3, 1333 MHz
	Chipset	NVIDIA nforce790i SLI	
VGA	GPU	NVIDIA G200 (GTX280)	Core 602 MHZ, Shader 1296 MHz
	Device RAM		1024 MB DDR3, 1107 MHz
Software & Drivers			
Operating System		Window XP 64 SP2	
Graphics Driver		ForceWare 257.21	
CUDA		V3.1	
Visual C++ 2005		V8.0.50727.762 SP1	-O2 -arch sm_13 -code sm_13

4.1 Rayleigh-Taylor instability (ref. to [14])

Using the proposed algorithm, the simulations running with one GPU core are limited to a resolution of 1024×4096 in double-precision mode. However, by paralleling 3 GPU cores, it is possible to achieve a maximum resolution of 1728×6912. Fig. 3 shows that the modified (2.5) achieves better enhancement than the prototype (2.3a).

Domain: $0 \leq x \leq 1/4$, $0 \leq y \leq 1$.

Boundary conditions:

- Both $x = 0$ and $x = 1/4$ are reflective boundaries.
- The bottom boundary $y = 0$ is fixed at the post-shock state.
- The top boundary $y = 1$ is fixed at the initial pre-shock state.

Table 2: Execution times for 4.1 Rayleigh-Taylor instability.

Resolution	Iteration	Computing Time (in sec.)	GPU Cores
240×960	8450	428.475	1
480×1920	16705	3355.210	1
960×3840	34136	26428.606	1
1728×6912	61044	48536.219	3

Equation of state: $\gamma = 5/3$.

Initial setup for interior grid points:

$$y \le \frac{1}{2},\ \text{post-shock state: } \begin{pmatrix} \rho \\ u \\ v \\ P \end{pmatrix} = \begin{pmatrix} 2 \\ 0 \\ -0.025 \cdot c_0 \cdot \cos(8\pi x) \\ 2y+1 \end{pmatrix},$$

$$\text{otherwise, pre-shock state: } \begin{pmatrix} \rho \\ u \\ v \\ P \end{pmatrix} = \begin{pmatrix} 1 \\ 0 \\ -0.025 \cdot c_0 \cdot \cos(8\pi x) \\ y+1.5 \end{pmatrix},\ \text{where } c_0 = \sqrt{\frac{\gamma P}{\rho}}.$$

CFL number: 0.475

Time period: $T = 1.95$

Source term: $s(\mathbf{U}) = (0, 0, \rho, \rho v)$

Fig. 4 presents the quantities $\mathbf{Q}^x_{i,j+1/2} + \mathbf{Q}^y_{i+1/2,j}$ for the three different formulas. The prototype (2.3a) achieves poor compensation (limited in individual x-direction or y-direction), but the modified (2.5) achieves a better performance close to (2.4) but without violating TVD. Because (2.4) is not TVD-restrained, its controversial demonstrations are bypassed in the following tests.

4.2 Double Mach reflection (ref. to [14])

Even though the time period of this example is too short to highlight differences between the various anti-diffusion terms, the modified formula (2.5) still performs better than the prototype (2.3a), as indicated in the "eye" area in Fig. 5.

Domain: $0 \le x \le 4, 0 \le y \le 1$

Boundary conditions:

- The left boundary $x = 0$ is fixed at the post-shock state.
- The right boundary $x = 4$ is fixed at the pre-shock state.
- The bottom boundary $y = 0$ is fixed at the post-shock state if $x \le 1/6$, otherwise is reflective.
- To describe the exact motion of shock, the top boundary $y = 1$ is fixed at the post-shock state if $x \le x_s(t)$, otherwise is fixed at the pre-shock state. Here $x_s(t) = 1/6 + (1 + 20t)/\sqrt{3}$.

Equation of state: $\gamma = 1.4$

Initial setup for interior grid points:

$$x \le \frac{1}{6} + \frac{y}{\sqrt{3}},\ \text{post-shock state: } \begin{pmatrix} \rho \\ u \\ v \\ P \end{pmatrix} = \begin{pmatrix} 8 \\ 8.25 \cdot \cos\left(\frac{\pi}{6}\right) \\ -8.25 \cdot \sin\left(\frac{\pi}{6}\right) \\ 1160.5 \end{pmatrix},$$

otherwise, pre-shock state: $(\rho, u, v, P) = (1.4, 0, 0, 1)$.

CFL number: 0.475

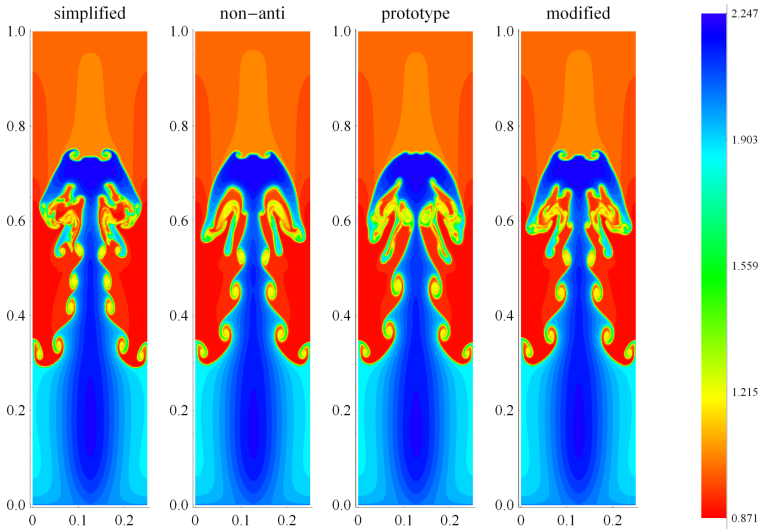

Figure 3: Rayleigh-Taylor Instability ($\Delta x = \Delta y = 1/6912$): Contours of density ρ using the same Kurganov algorithm with four different anti-diffusion terms. From left to right, the first one is from (2.4), the second has no anti-diffusion term as in [8], the third is from the prototype (2.3a) and the last one is from the modified formula (2.5).

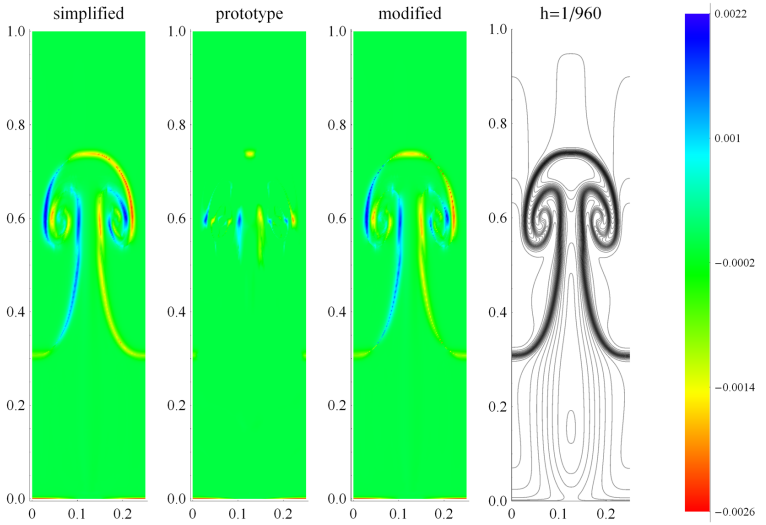

Figure 4: Rayleigh-Taylor Instability ($\Delta x = \Delta y = 1/960$): Images presenting the compensation quantities of different anti-diffusion terms. From left to right, the first one is from (2.4), the second is from the prototype (2.3a) and the third is from the modified formula (2.5). Compare these shapes with the simulated shock interfaces in the last figure.

Time period: $T = 0.2$

No source term: $s(\mathbf{U}) = (0, 0, 0, 0)$

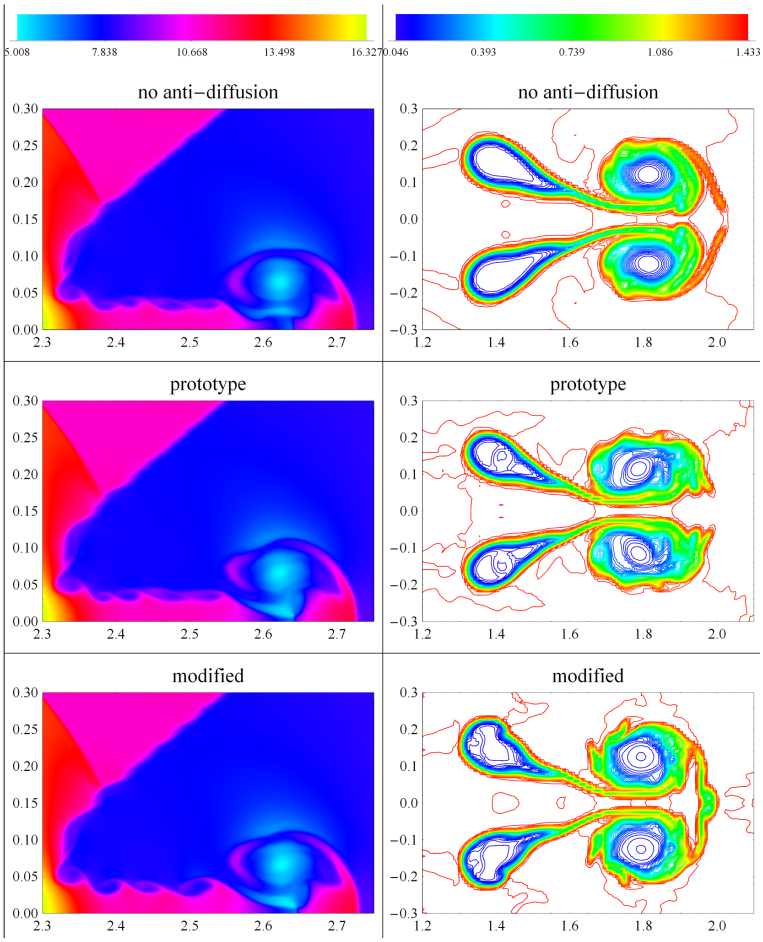

Figure 5: Figures on the right side are contours of density ρ for shock-bubble interaction problem ($\Delta x = \Delta y = 1/1200$) zoomed at $[1.2, 2.1] \times [-0.3, 0.3]$. Figures on the left side are density-plots of ρ for the Double Mach reflection problem ($\Delta x = \Delta y = 1/1728$) zoomed at $[2.3, 2.75] \times [0, 0.3]$. From top to bottom, the first one has no anti-diffusion term, the second is from the prototype (2.3a) and the last one is from the modified formula (2.5).

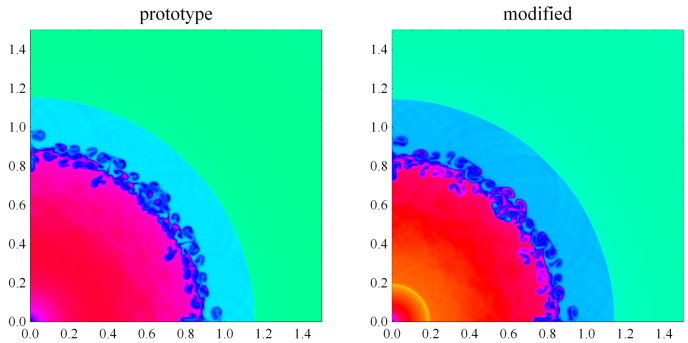

Figure 6: Explosion problem ($\Delta x = \Delta y = 1/2048$): Contours of density ρ.

4.3 Shock-bubble interaction (ref. to [2])

According to Fig. 5 and [2], formula (2.5) reduces the bubble splitting caused by numerical diffusion.

Domain: $-0.5 \leq x \leq 2.5$, $-0.5 \leq y \leq 0.5$

- Both $y = -0.5$ and $y = 0.5$ are reflective boundaries.
- Both $x = -0.5$ and $x = 2.5$ are outflow boundaries.

Equation of state: $\gamma = 1.4$

For the initial state of interior grid points, there is a vertical right-moving shock located at $x = -0.3$ and a circular bubble of radius 0.2 located at the origin:

$$(\rho, u, v, P) = \begin{cases} \left(\frac{4}{3}, \frac{707}{2000}, 0, 1.5\right), & x \leq -0.3, \\ \left(\frac{1}{29}, 0, 0, 1\right), & x^2 + y^2 \leq 0.04, \\ (1, 0, 0, 1), & \text{otherwise.} \end{cases}$$

CFL number: 0.475

Time period: $T = 4.0$

No source term: $s(\mathbf{U}) = (0, 0, 0, 0)$

4.4 Explosion (ref. to [2])

According to Fig. 6 and [2], the instabilities developed by (2.5) in the circular contact curve are "curlier".

Domain: $0 \leq x \leq 1.5$, $0 \leq y \leq 1.5$

- Both $y = 0$ and $x = 0$ are symmetric boundaries.
- Both $x = 1.5$ and $y = 1.5$ are outflow boundaries.

Equation of state: $\gamma = 1.4$

Initial setup for interior grid points:

$$(\rho, u, v, P) = \begin{cases} (1, 0, 0, 1), & x^2 + y^2 \leq 0.16, \\ (0.1, 0, 0, 0.1), & \text{otherwise.} \end{cases}$$

CFL number: 0.475

Time period: $T = 3.2$

No source term: $s(\mathbf{U}) = (0, 0, 0, 0)$

5 Conclusions

The demonstrated derivation addresses a defect in the 2D Kurganov scheme to reinforce its reduction of numerical dissipation for shock preserving in long-time, large-scale simulations. The experiments in this study reveal the effects of this modified 2^{nd}-order scheme. The proposed formula (2.5) is simple and clear and offers insights into the uncultivated 3D model.

Because of its amazing increase in speed, GPU computing is becoming increasingly popular for CFD simulations. Although several authors [1, 20, 21] have discussed this issue, the common problem of memory amount makes it difficult for most 3D GPU programs to achieve high resolution for each dimension. In the future, we think the enhanced anti-diffusion term will play a key role in the sophisticated large-scale simulations involving the 3D Kurganov scheme.

Acknowledgments

The authors thank Dr. Chi-Tien Lin (Department of Applied Mathematics, Providence University, Taiwan) for his guidance in finite volume methods and developing formula (2.4).

References

[1] A. ANTONIOU, K. KARANTASIS, E. POLYCHRONOPOULOS AND J. EKATERINARIS, *Acceleration of a finite-difference WENO scheme for large-scale simulations on many-core architectures*, 48th AIAA Aerospace Sciences Meeting Including the New Horizons Forum and Aerospace Exposition, 2010, AIAA Paper 2010-0525.

[2] A. KURGANOV AND C.-T. LIN, *On the reduction of numerical dissipation in central-upwind schemes*, Commun. Comput. Phys., 2 (2007), pp. 141–163.

[3] A. KURGANOV AND E. TADMOR, *New high-resolution central schemes for nonlinear conservation laws and convection-diffusion equations*, Comput. Phys., 160 (2000), pp. 241–282.

[4] A. KURGANOV AND E. TADMOR, *Solution of two-dimensional Riemann problems for gas dynamics without Riemann problem solvers*, Part. Diff. Equation., 18 (2002), pp. 584–608.

[5] A. KURGANOV AND D. LEVY, *Third-order semi-discrete central scheme for conservation laws and convection-diffusion equations*, SIAM J. Sci. Comput., 22 (2000), pp. 1461–1488.

[6] A. KURGANOV AND G. PETROVA, *Central schemes and contact discontinuities*, Numer. Anal., 34 (2000), pp. 1259–1275.

[7] A. KURGANOV AND G. PETROVA, *A third-order semi-discrete genuinely multidimensional central scheme for hyperbolic conservation laws and related problems*, Numer. Math., 88 (2001), pp. 683–729.

[8] A. KURGANOV, S. NOELLE AND G. PETROVA, *Semi-discrete central-upwind scheme for hyperbolic conservation laws and Hamilton-Jacobi equations*, SIAM J. Sci. Comput., 23 (2001), pp. 707–740.

[9] B. VAN LEER, *Upwind and high-resolution methods for compressible flow: from donor cell to residual-distribution schemes*, Commun. Comput. Phys., 1(2) (2006), pp. 192–206.

[10] C.-W. SHU, *High-order finite difference and finite volume WENO schemes and discontinuous Galerkin methods for CFD*, Int. J. Comput. Fluid. Dyn., 17 (2003), pp. 107–118.
[11] D. LEVY, G. PUPPO AND G. RUSSO, *Compact central WENO schemes for multidimensional conservation laws*, SIAM J. Sci. Comput., 22 (2000), pp. 656–672.
[12] G. S. JIANG, D. LEVY, C. T. LIN, S. OSHER AND E. TADMOR, *High-resolution nonoscillatory central schemes with nonstaggered grids for hyperbolic conservation laws*, SIAM J. Numer. Anal., 35 (1998), pp. 2147–2168.
[13] H. NESSYAHU AND E. TADMOR, *Non-oscillatory central differencing for hyperbolic conservation laws*, J. Comput. Phys., 87 (1990), pp. 408–463.
[14] J. SHI, Y.-T. ZHANG AND C.-W. SHU, *Resolution of high order WENO schemes for complicated flow structures*, J. Comput. Phys., 186 (2003), pp. 690–696.
[15] NVIDIA®, CUDA 2.0 Programming Guide. Available at `http://www.nvidia.com/object/cuda_develop.html`.
[16] NVIDIA®, CUDA ZONE. Available at `http://www.nvidia.com/object/cuda_home.html#`.
[17] S. GOTTLIEB AND C. W. SHU, *Total variation diminishing Runge-Kutta schemes*, Math. Comput., 67 (1998), pp. 73–85.
[18] S. GOTTLIEB, C. W. SHU AND E. TADMOR, *Strong stability-preserving high order time discretization methods*, SIAM Rev., 43 (2001), pp. 89–112.
[19] T. BRANDVIK AND G. PULLAN, *Acceleration of a 2D Euler flow solver using commodity graphics hardware*, J. Mech. Eng. Sci., 221 (2007), pp. 1745–1748.
[20] T. BRANDVIK AND G. PULLAN, *Acceleration of a 3D Euler solver using commodity graphics hardware*, 46th AIAA Aerospace Sciences Meeting and Exhibit, 2008, pp. 607.
[21] T. R. HAGEN, K.-A. LIE AND J. R. NATVIG, *Solving the Euler equations on graphics processing units*, in Computational Science-ICCS 2006, Vol. 3994 of LNCS, Springer, 2006, pp. 220–227.
[22] T. R. HAGEN, M. O. HENRIKSEN, J. M. HJELMERVIK AND K.-A. LIE, *How to solve systems of conservation laws numerically using the graphics processor as a high-performance computational engine*, in Geometric Modeling, Numerical Simulation and Optimization, Springer, 2007, pp. 211–264.